Electronic Supplementary Material (ESI) for Energy & Environmental Science.
This journal is © The Royal Society of Chemistry 2024

Electronic Supporting Information

Enhanced Bipolar Membrane for Durable Ampere-Level Water Electrolysis

Fen Luo[a, †], Weisheng Yu[a, †], Xiaojiang Li[a], Xian Liang[a], Wenfeng Li[a], Fanglin Duan[a], Yaoming Wang[a], Xiaolin Ge[a], Liang Wu*[,a], Tongwen Xu*[,a]

[a]. Key Laboratory of Precision and Intelligent Chemistry, Department of Applied Chemistry, School of Chemistry and Materials Science, University of Science and Technology of China, Hefei 230026, P. R. China.

Email: liangwu8@ustc.edu.cn; twxu@ustc.edu.cn.

† These authors contributed equally to this work.

Table of Contents

Experimental Section

Materials. P-Terphenyl, calix[4]arene (CA), 1-methyl-4-piperidone, 4-Vinylbenzyl chloride (VBC), iodomethane (CH_3I), 2,3-diketoindoline, trifluoromethanesulfonic acid (TFSA, 99%), dimethylamine (40%), formaldehyde (37%), biphenyl, trifluoroacetic acid (TFA, 99%), sodium hydride (NaH, disperse 60% in mineral oil), and 1,3-propanesultone (98%) were sourced from Energy Chemical Co. Ltd (Shanghai, China). Flake graphite (300 mesh, 99%) was procured from XFNANO Co. Ltd (Nanjing, China). M-Terphenyl was came from Aladdin. Nitric acid (HNO_3), potassium permanganate ($KMnO_4$), ammonium hydroxide ($NH_3{\cdot}H_2O$), sulfuric acid (H_2SO_4), hydrogen peroxide (H_2O_2), aqueous hydrazine hydrate solution ($N_2H_4{\cdot}H_2O$), hydrochloric acid (HCl), dichloromethane (CH_2Cl_2), potassium hydroxide (KOH), sodium hydroxide (NaOH), sodium chloride (NaCl), tetrahydrofuran (THF), acetic acid, diethyl ether, potassium carbonate (K_2CO_3), chloroform, methylene chloride (DCM), acetone, dimethyl sulfoxide (DMSO) and methanol (CH_3OH) were obtained from Sinopharm Chemical Co. Ltd (Shanghai, China). Pt black (Hispec9100, Johnson Matthey JM 60%), IrO_2 (SIr85, >85%), Nafion® D520 (5 wt% in ethanol) and Toray paper (TGP-H-60) was purchased from Sinero Co., Ltd., Suzhou, China. Deionized (DI) water (18.2 MΩ cm) in all experiments conducted in this study. Commercial Neosepta BPU (ASTOM R&D, Japan) was purchased and ultilized as the reference bipolar membrane.

Synthesis of sulfonated poly (biphenyl indole) (SPBI). The synthesis process of SPBI was adapted from previous work.[1] In a 500 mL round-bottom flask, 32.4 g of 2,3-diketoindoline, 30.8 g of biphenyl, and 40 mL of DCM were combined and stirred in an ice bath for 30 minutes. Subsequently, 30 mL of TFA and 70 mL of TFSA were added dropwise to the mixture. The reaction mixture was then stirred and cooled in the ice bath for an additional 6 hours before being poured into CH_3OH to precipitate the product. The solid precipitate was washed three times with CH_3OH, extracted, and dried at room temperature, resulting in the polymer poly(biphenyl indole) (PBI). Next, 80 g of PBI was dissolved in 800 mL of DMSO in a flask maintained at 60 °C. Gradually, 32 g of NaH was added to the solution, and the mixture was stirred at 60 °C for 3 hours. Afterward, 1.2 equivalents of 1,3-propanesultone were introduced, and the reaction was allowed to proceed for 12 hours at 80 °C. The mixture was then added dropwise into ether to precipitate the yellow solid, which was collected by filtration. The precipitate was washed with CH_3OH, and the final SPBI product was obtained after suction filtration and drying at room temperature. The ^{1}H NMR spectra of SPBI is shown in **Fig. S1**.

Manufacturing of poly (meta/para-terphenylene-methyl piperidinium) (MTCP-50) polymer. The synthesis procedure for MTCP-50 was adapted from previous research.[2] In a flask surrounded by an ice bath, 4.6 g of m-Terphenyl and 4.6 g of p-Terphenyl were combined, followed by the rapid injection of 1-methyl-4-piperidone (4.97 g) and CH_2Cl_2 (4 mL). Subsequently, 1.6 mL of TFA and 20 mL of TFSA were added dropwise, and the reaction mixture was stirred continuously in the ice bath for 9 hours. The resulting mixture was then poured into a 2 mol L^{-1} NaOH solution and stirred vigorously for 48 hours. After repetitive washing with deionized (DI) water, the MTP-50 was obtained through filtration and drying at 60 °C. Finally, a round-bottom flask was charged with 2.6 g of MTP, 0.33 g of K_2CO_3, 0.122 g of VBC, and 18 mL of DMSO. The mixture was stirred at room temperature for 24 hours, after which an excess of CH_3I was added to carry out the quaternary ammonium reaction for an additional 12 hours with continuous stirring. The resulting homogeneous solution was poured into acetone to precipitate the product, which was then washed with DI water and air-dried. The ^{1}H NMR spectra of the obtained MTCP-50 is shown in **Fig. S2**.

Preparation of graphene oxide (GO). GO was synthesized according to the modified Hummers' method.[3] In a typical synthesis procedure, 3 g of graphite flakes were added to a round-bottom flask containing a mixture of HNO_3 and H_2SO_4 (40/360 mL). After stirring for 20 minutes, 18 g of $KmnO_4$ was slowly introduced into the flask while stirring in an ice bath. The reaction was then transferred to an oil bath at 50 °C and stirred for 12 hours. The reaction solution was subsequently diluted with 500 mL of iced water, and 10 mL of 30% H_2O_2 was added gradually to completely react with the residual $KmnO_4$. Once cooled to room temperature, the suspension was washed with HCl solution (37%) and deionized water until neutral. After each wash, the suspension was centrifuged at 8000 rpm for 30 minutes, and the supernatant was discarded. Finally, the neutral suspension was filtered using cellulose membranes and dried in a freeze dryer for 24 hours.

Synthesis of 4-tertiary amine calix[4]arene (NCA). The NCA was synthesized following a previously reported method.[4] Briefly, to a solution of CA (0.0025 mol, 1.0827 g) in THF (23 mL), we added 40% dimethylamine aqueous (0.0126 mol, 1.42 g), acetic acid (2.8 mL) and 37% formaldehyde aqueous (0.0126 mol, 1.02 g). The mixture was stirred for 24 h at room temperature. After stirring, the reaction was filtered under vacuum, and the residue was redissolved in 16 mL of deionized water. The resutling solution was extracted twice with ether (200 mL) and neutralized with 10% K_2CO_3 solution. The formed precipitate was collected via suction filtration. Finnaly, the product was dried and recrystallized from chloroform, and the ^{1}H NMR of synthesized NCA is shown in **Fig. S3**.

Fabrication of 4-tertiary amine calix[4]arene-modified graphene oxide (GO-NCA). For the modification of GO with NCA, we followed procedures based on previous reports.[5] Initially, 0.05 g of GO and 0.1 g of NCA were dispersed in 40 mL of deionized water via ultrasonication for 2 hours. To the mixture, 20 µL of aqueous hydrazine hydrate solution and 200 µL of ammonium hydroxide were added, and the mixture was stirred at 60 °C for 4 h. The GO-NCA was then collected by vacuum filtration.

Fabrication of bipolar membranes. As shown in **Fig. S4**, both the CEL and AEL exhibit exceptional dimensional stability and appreciable H^+ and OH^- conductivity, making them ideal materials for BPM fabrication. To address the interpenetration issue between the CEL and AEL layers and to precisely control the catalyst loading and membrane layer thickness, an ultrasonic full-spraying method was adopted for BPM fabrication. Fully sprayed BPMs containing GO or GO-NCA catalysts were fabricated and referred to as GO@BPM and GO-NCA@BPM, respectively. For example, the fabrication of a GO-NCA@BPM with a 15 µg cm^{-2} loading of GO-NCA catalyst, a 15-µm-thick CEL, and a 17-

μm-thick AEL involved three main steps: (1) SPBI polymer (0.1 g) was dissolved in 1 g of DMSO at 60 °C and then diluted with 2 g of CH_3OH to form a homogenous cation-exchange polymer solution (3.2%). The clear supernatant was extracted via centrifugation, and the solution was sprayed onto a 5×5 cm clean glass substrate at 85 °C using an ultrasonic spraying machine (USD-220P-FS/T, Nasonic Ultrasound Technology Co. Ltd, Suzhou, China) for 30 cycles at a flow rate of 0.4 mL min^{-1}. A CEL of approximately 15 μm thickness was obtained after drying for 30 minutes; (2) GO-NCA catalysts (19 mg) were uniformly dispersed in 100 mL of DI water using ultrasonication to prepare a catalyst ink (0.19 mg mL^{-1}). This ink was then sprayed onto the CEL with a loading 15 μg cm^{-2} using ultrasonic spraying for 20 cycles at a flow rate of 0.2 mL min^{-1}; (3) The MTCP-50 polymer (1 g) was dissolved in 6 g of DMSO and then diluted with 13 g of CH_3OH to form a uniform AEL solution. After centrifugation, the AEL solution was spray-coated onto the CEL for 32 cycles at a flow rate of 0.4 mL min^{-1}, completely covering the catalyst layer. The AEL with a thickness of 17 μm was completed after drying for 30 minutes. The fully sprayed BPM was obtained by soaking in DI water and detaching it from the glass plates. For BPMs with different thicknesses or catalyst loadings, adjustments can be made by carying the number of spraying cycles for corresponding solutions.

Basic quality determination of AEL and CEL.

Ionic conductivity. The in-plane conductivity of the CEL in H^+ form and the AEL in OH^- form was measured using a four-electrode platinum setup with an AC impedance analyzer (Zahner Zennium E). Both the AEL and CEL samples were cut into dimensions of 1×4 cm. The thickness (d) and width (W) of the samples were quickly determined using a spiral micrometer and a graduated scale, respectively. The samples were then placed into a measurement cell fully immersed in deionized (DI) water, with the distance (L) between the two potential sensing electrodes set to 1 cm. Impedance measurements were carried out at a specified temperature over a frequency range from 1 MHz to 100 Hz to obtain the in-plane ohmic resistance ®. The ionic conductivity (σ) was calculated using the following equation:

$$\sigma = \frac{L}{RWd} \ (S1)$$

Water uptake (WU) and swelling ratio (SR). The WU and SR measurements of AEL in OH^- form and CEL in H^+ form were achieved by soaking in corresponding NaOH (1 M) and HCl (1 M) for 24 h to transform counterions into OH^- and H^+. Both of the samples were washed thoroughly with water for many times until the water was neutral followed by drying at 60 °C for 12 h to obtain the weight (W_{dry}) as well as length (L_{dry}). Then the samples were immersed in water for 12 h at different temperature. The wet weight (W_{wet}) as well as length (L_{wet}) of solvated samples were recorded after wiping the excess surface water. Each measurement was performed three times applying different samples to avoid experimental errors. The WU and SR were calculated from below equation:

$$WU(T)(\%) = \frac{W_{wet}(T) - W_{dry}}{W_{dry}} \times 100\% \ (S2)$$

$$SR(T)(\%) = \frac{L_{wet}(T) - L_{dry}}{L_{dry}} \times 100\% \quad (S3)$$

Ion exchange capacity (IEC). The IEC value of CEL was determined using the classical acid-base titration method. Typically, CEL samples were immersed in a 1 M HCl aqueous solution for 24 hours to convert them into the H^+ form. The samples were then repeatedly rinsed with deionized (DI) water to remove any residual HCl. After thorough drying at 60 °C, the weight of the dried samples in the H^+ form (W_{dry}, g) was recorded. Subsequently, the samples were transferred into a 1 M NaCl aqueous solution and left for 24 hours at room temperature. The displaced H^+ ions were titrated with a 0.01 M NaOH aqueous solution using phenolphthalein as an indicator. For AEL samples, the IEC measurement was performed using the Mohr titration method. The AEL samples were ion-exchanged in a 1 M NaCl aqueous solution for 24 hours to switch them to the Cl^- form. After multiple rinses with DI water, the samples were dried at 60 °C, and the weight of the dried samples in the Cl^- form (W_{dry}, g) were recorded. The samples were then transferred into a 0.5 M Na_2SO_4 aqueous solution for another ion exchange at room temperature for 24 hours. Finally, the solution was titrated with a 0.01 M $AgNO_3$ solution using K_2CrO_4 as the colorimetric indicator. The IEC values were calculated as follows:

$$\mathrm{IEC} = \frac{V_{NaOH/AgNO_3} \times C_{NaOH/AgNO_3}}{W_{dry}} \ (S4)$$

Where W_{dry} is the dry weight of CEL/AEL, $V_{NaOH/AgNO_3}$ is the consumed volume of the NaOH/$AgNO_3$ solution, and $C_{NaOH/AgNO_3}$ is the concentration of the NaOH/$AgNO_3$ solution.

Chemical structure analysis. The chemical structures of the SPBI and MTCP ionomers were identified through ^{1}H Nuclear Magnetic Resonance (^{1}H NMR, Bruker 510, 400 MHz)

Microscopy analysis.

Field-emission scanning electron microscopy (FE-SEM, Gemini SEM 500, ZEISS, Germany) analysis. FE-SEM was ultilized to analyze samples featuring the surface of CEL and CEL coated with GO or GO-NCA catalysts, and the cross-sections of BPMs to investigate their morphologies. For cross-sectional samples, they were fractured in liquid nitrogen, and all samples were coated with Pt prior to test. An energy dispersive spectroscopy detector (EDS, Silicon Drift Detector (SDD)-X-MaxN, OXFORD) was employed to analyze the element distribution through the cross-section.

Atomic force microscopy (AFM, Dimension Icon, Bruker) analysis. The AFM was conducted in tapping mode to study the morphology of the membranes and the catalysts. Additionally, Kelvin Probe Force (KPFM) was also used to determine the work function (WF) and Fermi level of the membranes. For better interpretation, the resulting data was processed with NanoScope Analysis software 1.8 (Bruker Corporation, USA), and the contact potential difference (CPD) and the WF were calculated as follows:

$$\mathrm{CPD} = \frac{\emptyset_{tip} - \emptyset_{sample}}{e} \quad (S5)$$

$$\emptyset_{\mathrm{sample2}} - \emptyset_{\mathrm{sample1}} = (\mathrm{CPD}_1 - \mathrm{CPD}_2) \times \mathrm{e} \quad (S6)$$

Where $\emptyset_{tip}$ and $\emptyset_{sample}$ represent the WF of the scanning probe and membrane surface, respectively, and e is the elementary charge.[6]

Transmission electron microscopy (TEM) analysis. TEM images were collected using JEM 2100F field-emission TEM (JEOL Ltd., Akishima, Tokyo, Japan) to observe the morphology of catalysts. Energy Dispersive Spectrometer (EDS) was combined with TEM to analyze the element distribution.

X-ray photoelectron spectroscopy (XPS). X-ray photoelectron spectroscopy (XPS, ESCALAB 250, Thermo-VG Scientific, USA) was conducted using Al Kα radiation to confirm the successful synthesis of GO-NCA.

X-ray diffraction analysis (XRD). X-ray diffraction (XRD) spectra (Tokyo, Japan) were recorded with Cu Kα radiation in the 2θ range of 5-30 degrees at a scan rate of 10° min^{-1} to determine the layer spacing of GO and GO-NCA.

Water contact angle. The water contact angle of the membranes with different catalysts was measured through a contact angle goniometer (SL200B, Solon Tech. Shanghai Co., Ltd.) to explore the surface hydrophilicity difference.

Cyclic voltammogram (CV) profiles. The double-layer capacitance of the two catalysts (GO and GO-NCA) was evaluated from cyclic voltammetry (CV) curves obtained using a standard three-electrode system at different voltage scan rates (50, 100, 150, 200 mV sec^{-1}) in a 0.5 M KCl electrolyte on an electrochemical workstation (CHI7052E). The working electrode was a catalyst-coated hydrophilic carbon paper, a Pt plate served as the counter electrode, and an Ag/AgCl electrode was used as the reference electrode. The double-layer capacitance (C_{dl}) was calculated using the following equation:[7]

$$C_{dl} = \frac{dj}{dV/dt} \quad (S7)$$

$$dj = J_a - J_c \quad (S8)$$

Where J_a and J_c are the anode and cathode current densities, dV/dt is the voltage scan rate.

Electrochemical WD performance, selectivity.

Measurements of BPM water dissociation ability at low current density. The WD test was conducted under reverse bias potential in a four-electrode cell with Luggin capillary design (Fig. S13a). Before measurements, the BPMs were equilibrated in 0.5 M Na_2SO_4 test solution for 24 h. Two platinum sheet electrodes were worked as the working and counter electrodes, whereas the Ag/AgCl electrodes were connected to the sensor and reference electrodes through Luggin capillary. Then the current-voltage (I-V) curves were collected using Autolab workstation (PGSTAT 302 N, Metrohm, Netherland) controlled by Nova 2.1.2 software with a current range from 0 to 0.35 A and the scan rate of 2 mA s^{-1}. The test solution was 0.5 M Na_2SO_4 or 1 M acid/base (0.5 M H_2SO_4/1 M KOH) unsymmetrical electrolytes.

Determination of BPM water dissociation capability at high current density. The I-V data at high current density was recorded using a similar four-electrode device as described earlier. Due to the limitation of the Autolab workstation, a constant galvanostatic current was supplied by a DC power source (HSPY-300-03, Hansheng Puyuan Co., Ltd., China), connected to the working and counter electrodes through platinum contacts. Two Ag/AgCl reference electrodes, positioned one millimeter away from the BPM's surfaces via Luggin capillaries, were connected to a digital multimeter (VC990F, VICTOR) to measure the transmembrane voltage drop (Fig. S13b).

Measurements of BPM selectivity. The selectivity of BPMs was determined by the first limiting current density of WD, derived from the first-order derivative of the I-V curves (dV/dI) with respect to current density.

Electrochemical impedance spectroscopy (EIS) analysis of BPMs. Galvanostatic electrochemical impedance spectroscopy (EIS) tests were conducted using the same setup (Fig. S13a) to evaluate junction capacitance, junction thickness, and WD resistance. EIS measurements were performed at 20 mA cm^{-2} in FRA impedance galvanostatic mode with a frequency from 10^5 to 0.1 Hz. Each empirical data was acquired from the average of 10 acquisition points and represented in typical Bode and Nyquist plots. According to the equivalent circuit, the Nyquist plot fitting, done using Z-view software, provided parameters such as ohmic resistancethe (R_Ω), WD rate constant (k_d), resistance of WD (R_{WDR}), time for ions migration out of depletion layer (τ_{tr}) and electric field intensity (E). the caculations use the following calculation formulas:

$$\lambda = \frac{\varepsilon_0 \varepsilon_r A_{ef}}{C} \quad (S9)$$

$$C = R_{WDR}^{(1-n)/n} Q_{DL}^{1/n} \quad (S10)$$

$$\frac{k_d(E)_{SWE}}{k_d(0)_{SWE}} = (\frac{2}{\pi})^{0.5} 8b^{-0.75} e^{(8b)^{0.5}} \quad (S11)$$

$$b = 0.09636 \frac{E}{\varepsilon_r T^2} \quad (S12)$$

Where ε_0 and ε_r are the dielectric constant of vacuum (8.854×10^{-12} F m^{-1}) and the sample (80 F m^{-1} for pure water), respectively, A_{ef} is the effective contact area (3.14 cm^2); C is the depletion capacitance; R_{WDR} indicates the impedance of BPM water dissociation; Q_{DL} and n

represent the quasi-capacitance (CPE-T) and CPE order (CPE-P), respectively; and CPE is constant phase. The $k_d(E)_{SWE}$ and $k_d(0)_{SWE}$ are the WD rate constants with and without an electric field under the second Wien effect (SWE) mechanism, respectively.

BPM water electrolysis.

Preparation of anode and cathode gas-diffusion layers (GDLs). The anode and cathode were prepared following previous reports.[8] Typically, the gas-diffusion layers (GDLs) were fabricated through spray coating. For cathode catalyst ink, 27.1 mg of Pt black (Hispec9100, Johnson Matthey JM 60%) were dispersed in a mixed solution of 0.41 g water, 0.46 g isopropyl alcohol and 2.7 mg Nafion® D520 (5 wt% in ethanol). For the anode catalyst ink, 2 mg of IrO_2 (SIr85) were dispersed in a mixture of 0.1 g water, 0.35 g isopropyl alcohol and 2 mg MTCP solution (5 wt% in DMSO). After thorough dispersion, the cathode and anode catalyst inks were sprayed onto a 2.5×2.5 cm^2 Toray paper (TGP-H-60) to fabricate the GDLs until a loading of 2 mg cm^{-2} was achieved.

Electrolyzer measurements. Pure water electrolysis and acid-base electrolysis were performed using a bipolar-membrane-electrode assembly (MEA) integrating electrodes and membranes into an electrolysis setup. Firstly, the gasket and the cathode GDL containing Pt catalysts were placed sequentially on a corrosion-resistant titanium back plates with graphite serpentine flow channels for water supply and gas transport. Then the BPM, gasket and the anode GDL with IrO_2 catalysts were stacked in sequence to ensure a wrinkle-free interface, with the CEL in contact with cathode GDL and the AEL toward anode GDL. Finally, another set of titanium plates with serpentine flow channels were placed on top, and the entire MEA was tightened with screws evenly spaced at the edges using a torque wrench. Polarization curves were recorded using a LANHE battery test station while feeding the MEA with either pure water or acid-base solutions (0.5 M H_2SO_4 for cathode and 1 M KOH for anode) at 80 °C. For long-term WD stability tests, the temperature was set to 60 °C.

Faradic efficiency (FE) and gas collection of BPMs. The determination of H_2 and O_2 Faradaic efficiencies (FE) was performed at a current density of 500 mA cm^{-2} using a membrane electrode assembly (MEA) fed with either pure water or an acid-base solution at room temperature. The measurement procedure was consistent with the previously mentioned water electrolysis test, and gas collection was carried out using the drainage and gas collection method. The FE for H_2 and O_2 was calculated based on the following formula:

$$\mathrm{FE} = \frac{\mathrm{n_{actual}}}{\mathrm{n_{theoretical}}} \times 100\% \quad \text{(S13)}$$

$$n_{H_2} = \frac{I \times t}{F} \times \frac{1}{2} \quad \text{(S14)}$$

$$n_{O_2} = \frac{I \times t}{F} \times \frac{1}{4} \quad \text{(S15)}$$

$$PV = nRT \quad \text{(S16)}$$

Where *I* is the current applied to the system (A), *t* is the reaction time (s), *F* is the Faradic constant, *P* is the atmospheric pressure (1.013×10^5 Pa), *V* is the volume of gas generated (m^3), *R* is the ideal gas constant, and *T* is the temperature (K).

Model description. The electrochemical potential distribution and the fluxes of mobile ions are described by the Nernst-Planck equation:[9]

$$\nabla(-D_i\nabla C_i - z_i u_i F c_i \nabla V) = R_i \quad \text{(S17)}$$

$$\nabla(\varepsilon\varepsilon_0 E) = \rho_v \quad \text{(S18)}$$

Where ε and ε_0 represent the relative dielectric constant and the vacuum permittivity, respectively. The value of ε_0 is 8.854×10^{-12} F m^{-1}, and ε is taken to be 80 for water. *E* is the electric field, and ρ_v is the net space charge density resulting from the concentration difference between anions and cations. *V* is the potential, and its gradient represents the electric field. Parameters D_i, C_i, u_i and z_i represent the diffusion coefficient, concentration, mobility, and charge of species i, respectively. In equation 17, R_i signifies the generation term accounting for concerntration changes due to the chemical reaction. In this model, BPMs under reverse bias generate H^+ and OH^- through WD, while the amount of supporting electrolyte is assumed to remain constant. The generation terms for H^+ and OH^- are given by:

$$R_i = k_d C_{\mathrm{H_2O}} - k_b C_{H^+} C_{OH^-} \quad \text{(S19)}$$

Where k_d represents the WD rate constant, while the k_b is the recombination rate constant.

To model the water transport in membranes, water is assumed to be fed on both sides, ensuring its presence at the outer BPM boundaries. According to the equation proposed by Weber and Newman, the relationship between water content and concentration is expressed as follows:[10]

$$\lambda = \frac{\frac{EW}{\rho^{dry}}}{\frac{1}{c} - \frac{M_{H_2O}}{\rho_L}} \quad \text{(S20)}$$

Where λ is the moles of water per mole of ion sites, ρ^{dry} is the density of dry CEM and AEM, and EW represents the equivalent membrane weight. Additionally, M_{H_2O} is the molar weight of water, and ρ_L represents the density of liquid water. For clarity, water content is used instead of water concentration. Water diffuses into the interlayer driven by gradients in water content. Positive direction is defined as towards the interlayer, which is favorable for WD, whereas the negative direction is defined where H^+ and OH^- drag water from the interlayer to the outer boundaries. Steady-state water balance conditions are calculated using the following equation:

$$0 = \frac{dc}{dt} = \frac{d}{dx}\left(N^{diff} + N^{drag}\right) \quad (13)$$

$$N_{AEM}^{diff} = -D^{AEM}(\lambda_{AEM})\frac{dc}{dx} \quad (14)$$

$$N_{CEM}^{diff} = D^{CEM}(\lambda_{CEM})\frac{dc}{dx} \quad (15)$$

$$N_{AEM/CEM}^{drag} = -n^{drag,\frac{AEM}{CEM}}\left(\lambda_{\frac{AEM}{CEM}}\right)\frac{i_{\frac{OH^-}{H^+}}}{F} \quad (16)$$

Where N^{diff} and N^{drag} represent the diffusive flux and electro-osmotic drag fluxes, respectively, which are linearly superimposed.

Supporting discussions

Advantages of BPM electrolyzers. Compared to AEMWEs and PEMWEs, BPMWEs offer distinct advantages attributed to their unique structure and specialized capacity for *in-situ* generation of H^+ and OH^- ions. Key advantages include:

(1) **Cost-effective catalysts usage:** BPMWEs allow for the use of affordable, alkaline-compatible catalysts (e.g., Fe-, Ni-, and Co-based catalysts) for the OER in an alkaline environment, while efficiently facilitating the HER at an acidic cathode. This dual-environment configuration reduces dependency on expensive noble-metal catalysts like IrO_2, typically required in acidic PEMWEs.[11]

(2) **Optimized reaction kinetics:** BPMWEs matain a steady-state pH gradient across the membrane, enabling optimal kinetics for electrode reactions. This unique capability enables HER at the acidic cathode and OER at the alkaline anode, offering greater versatility and stablility than AEMWEs and PEMWEs, which generally operate under fully alkaline or acidic conditions.

(3) **Enhanced durability and minimized degradation:** AEMWEs and PEMWEs often rely on external alkaline or acidic solutions, which can reduce reaction kinetics at the cathode or anode and accelerate electrolyzer degradation. Conversely, BPMWEs present notable benefits for pure water electrolysis, as they can function without additional alkaline or acidic feed solutions, thanks to their *in-situ* generation of H^+ and OH^- ions. This distinctive feature not only streamlines the system but also optimizes electrode reaction kinetics, promoting prolonged operation.

In summary, BPMWEs excel in cost-effective catalyst utilization, optimized reaction kinetics, and durability, making them a highly efficient and versatile alternative to AEMWEs and PEMWEs for water electrolysis. While BPMWEs in this study require further enhancement to compete with AEMWEs, which can achieve current densities of up to 10 A cm^{-2} under similar voltage, there is strong potential for BPMWEs to match or exceed the efficiency of AEMWEs and PEMWEs with future advancements in membrane conductivity, ionomer selection, catalyst efficiency, and porous transport layer design.[12]

Figures and Table

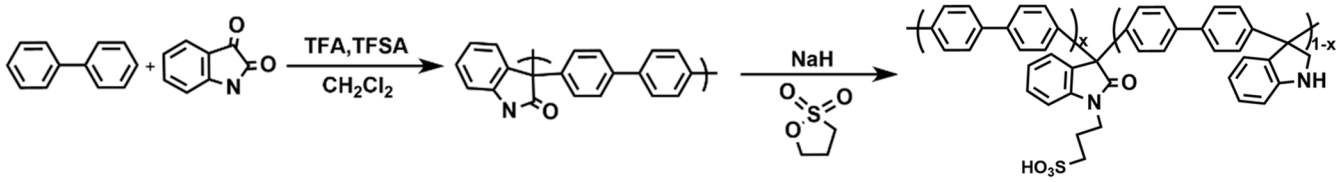

Scheme S1. Synthesis of sulfonated poly (biphenyl indole) (SPBI).

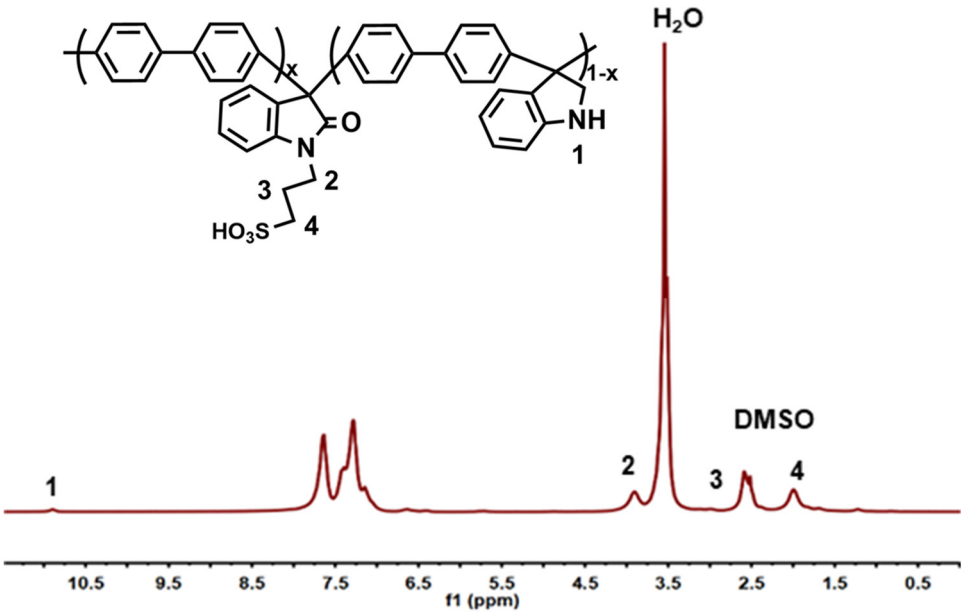

Fig. S1. ^{1}H NMR spectrum of SPBI.

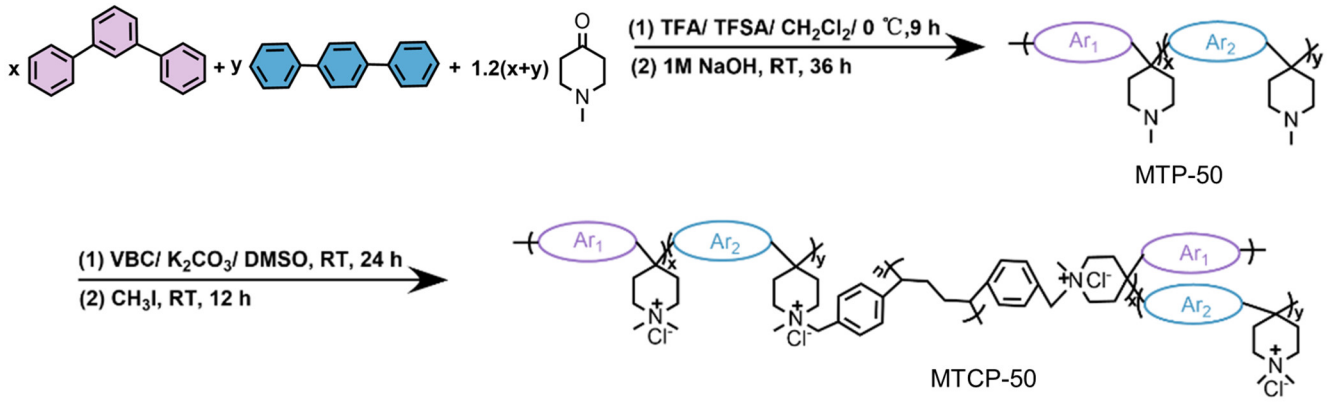

Scheme S2. Synthesis of MTCP-50 polymer.

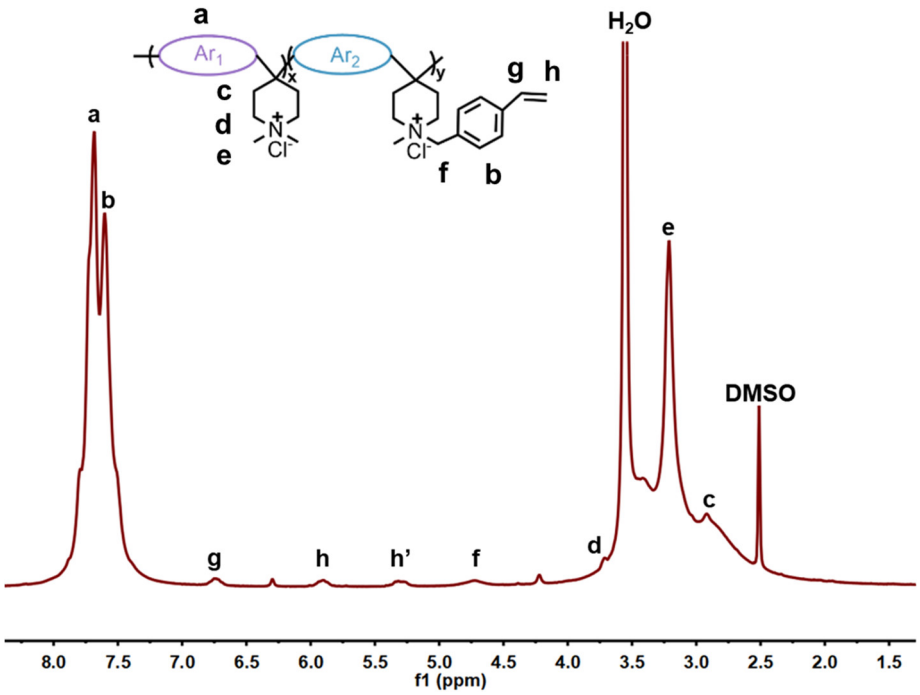

Fig. S2. ^{1}H NMR spectrum of MTCP-50.

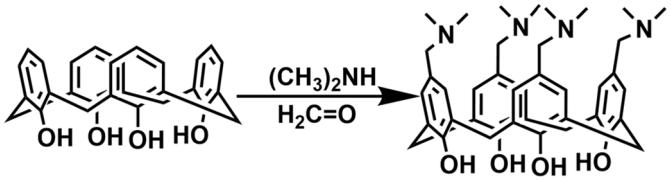

Scheme S3. Synthesis of 4-tertiary amine calix[4]arene (NCA).

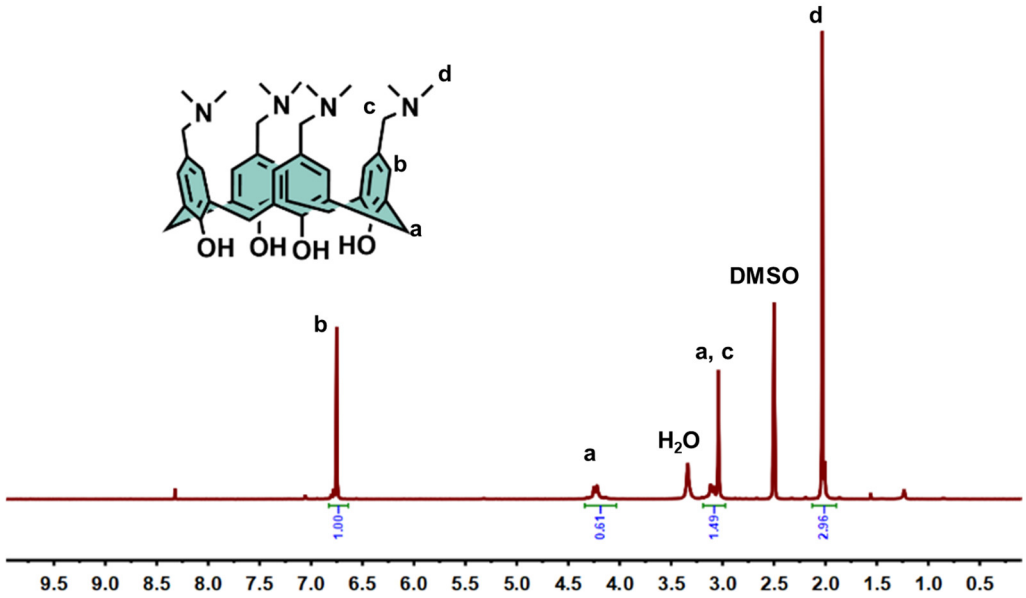

Fig. S3. ^{1}H NMR spectrum of NCA.

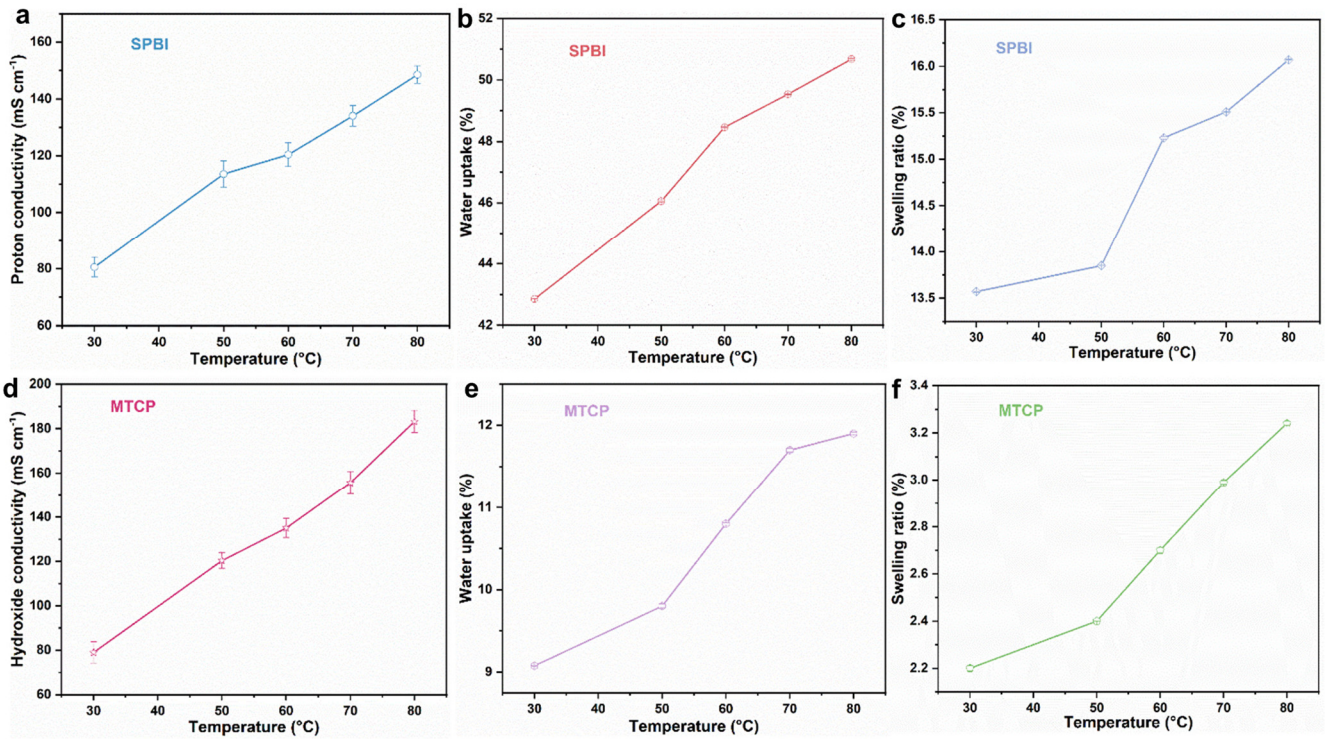

Fig. S4. Fundamental characteristics of CEL and AEL vs. temperature. Conductivity of CEL (a) and AEL (d). Water uptake of CEL (b) and AEL (e). Conductivity of CEL (c) and AEL (f). The CEL (SPBI) and AEL (MTCP) exhibit appreciable H^+ and OH^- conductivities of 148.7 and 183.7 mS cm^{-1} at 80 °C, respectively. The AEL presents excellent high-temperature tolerance with a swelling ratio of less than 5.0% at room temperature and even at 80 °C. However, the dimensional stability of CEL remains to be further improved because the water uptake and swelling ratio of CEL appear to be slightly high in the present.

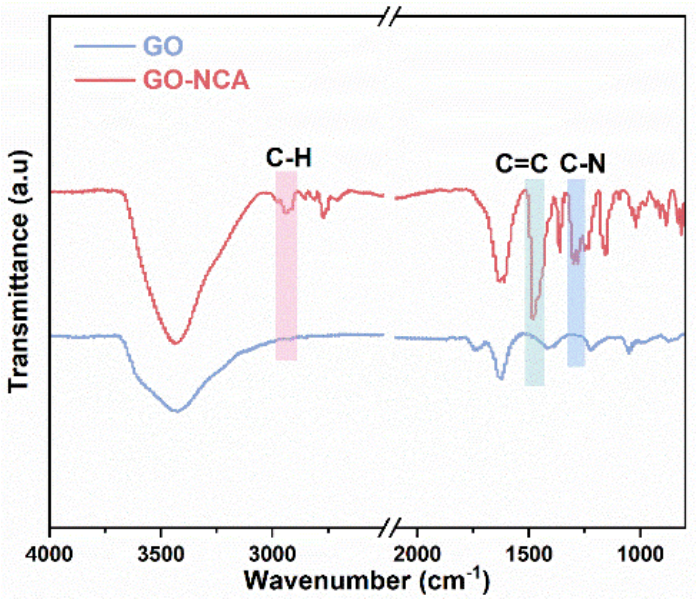

Fig. S5. FTIR spectra of GO and GO-NCA catalysts. The three newly emerged signal peaks belong to the NCA molecules. The strong water adsorption peak at 3376 cm^{-1} in the drying samples indicates the hydrophilic nature of the catalysts.

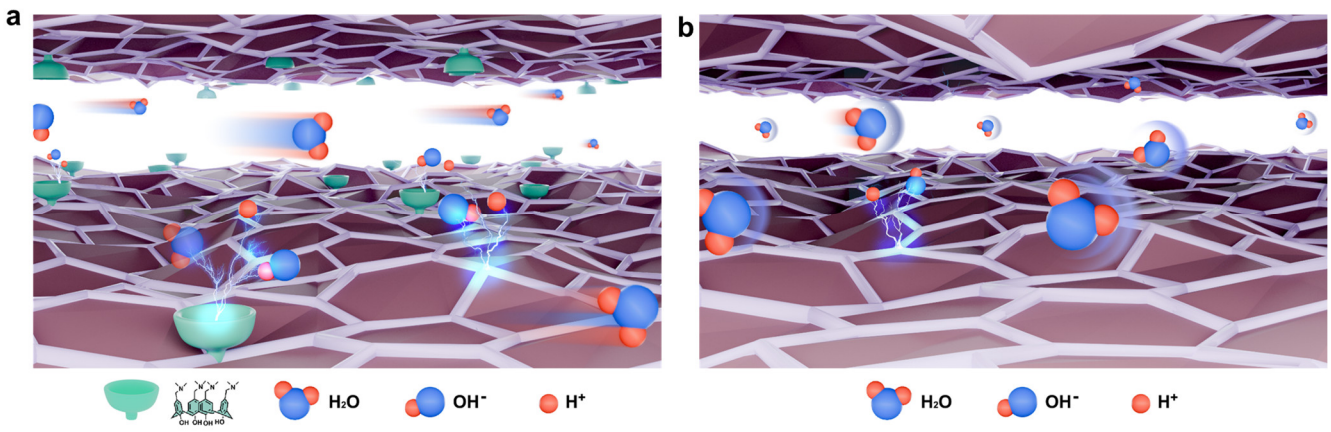

Fig. S6. Schematic diagram of water molecules transport and dissociation in interlayer channels of (a) GO-NCA and (b) GO.

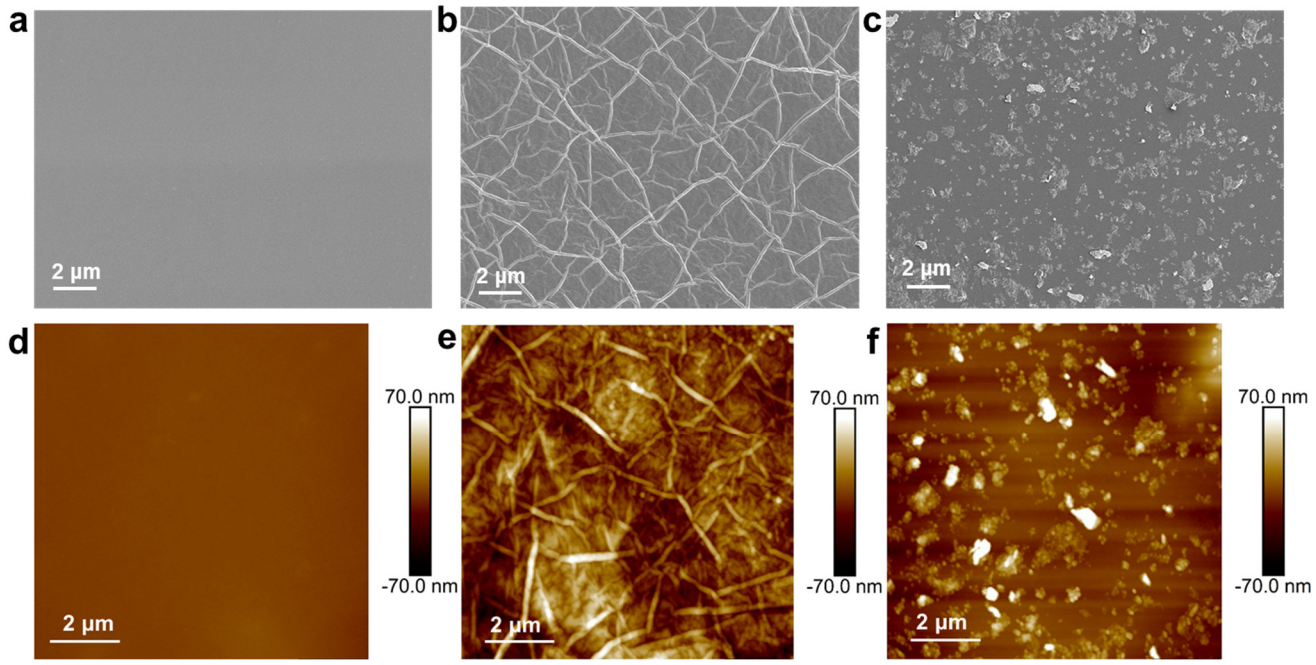

Fig. S7. Morphological characteristics of WD catalytic layer. (a-c) Surface SEM micrographs of original CEL, CEL sprayed with GO (4.56 μg cm^{-2}) and GO-NCA (9.12 μg cm^{-2}), respectively. (d-f) AFM images of original CEL, CEL sprayed with GO and GO-NCA, respectively.

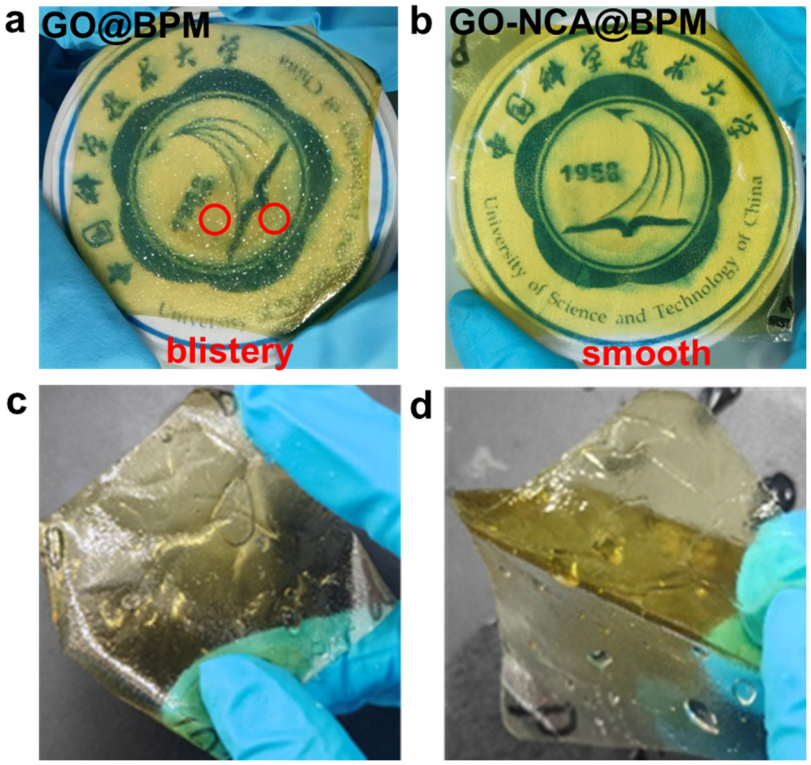

Fig. S8. Photographs of the (a) GO@BPM and (b) GO-NCA@BPM after soaking in water for 24 hours. The GO@BPM and GO-NCA@BPM are fabricated via the proposed full spraying method. The GO@BPM could not remain stable in water with the appearance of blisters. Whereas, the GO-NCA@BPM remained highly stable with a smooth surface. (c-d) Digital photographs of GO@BPM with the loading of 5 μg cm^{-2} immersed in water for a minute. An obvious phenomenon of AEL and CEL stratification can be observed.

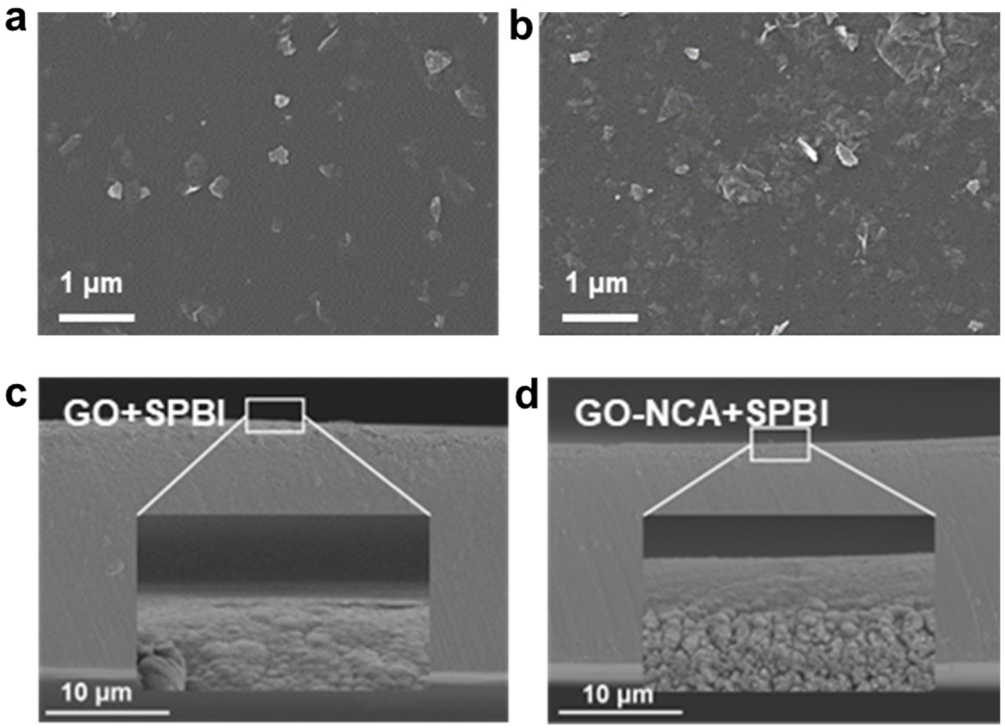

Fig. S9. (a-b) Surface SEM micrographs of CEL covering GO-NCA with the load of 4.56 μg cm^{-2} and 15.2 μg cm^{-2}, respectively. (c-d) SEM cross-sectional images of CEL spraying GO-NCA (4.56 μg cm^{-2}) and GO-NCA (9.12 μg cm^{-2}), respectively.

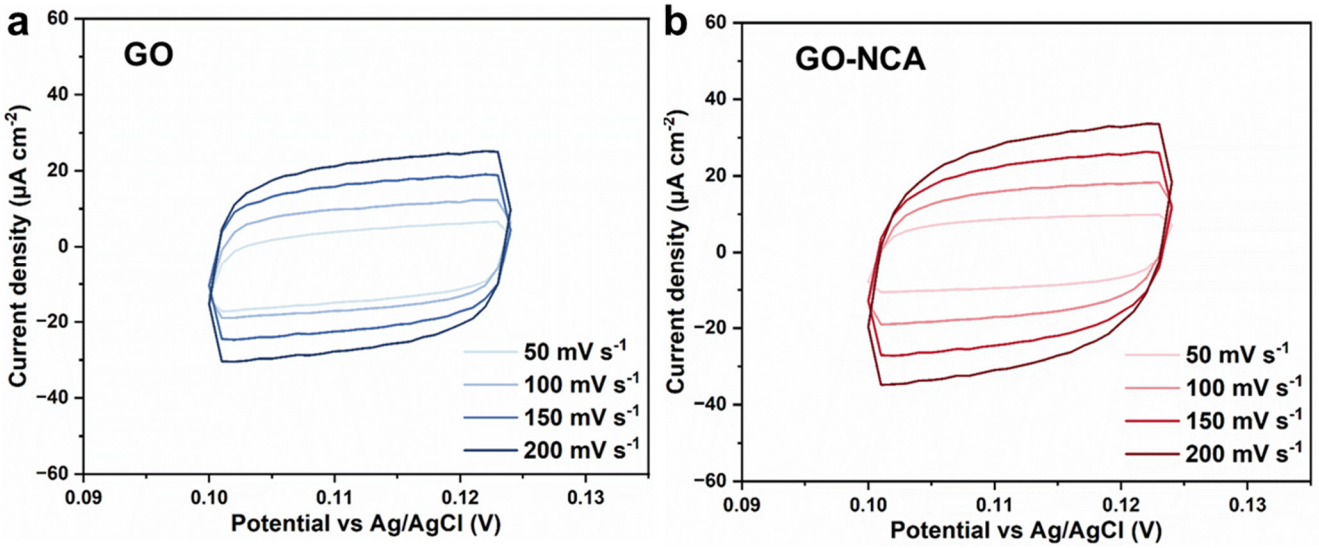

Fig. S10. Cyclic voltammetry curves of (a) GO and (b) GO-NCA catalysts tested in 0.5 M KCl at diverse voltage scan rates.

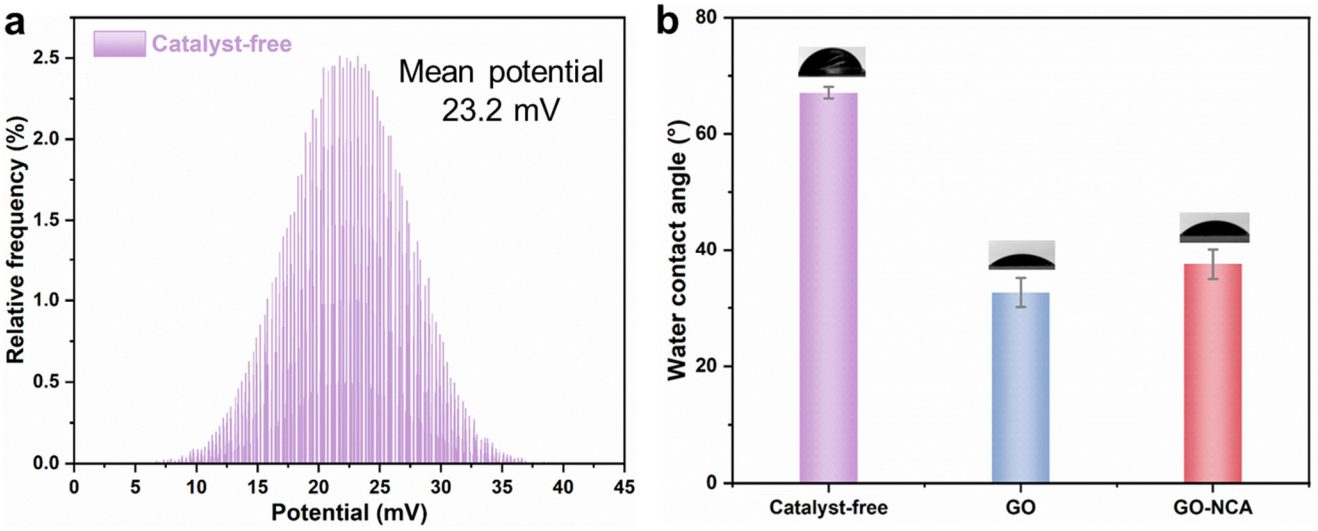

Fig. S11. (a) The Gauss statistic distribution histograms of contact potential difference for CEL surface. (b) The water contact angle of CEL, CEL surface sprayed with GO, and GO-NCA.

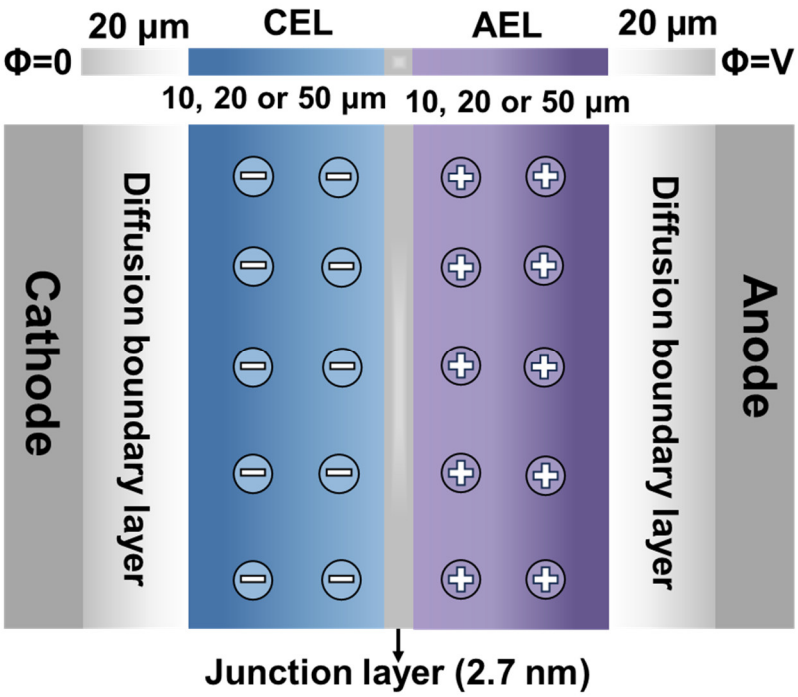

Fig. S12. Schematic illustration of 1-D BPM model in H-cell system for numerical simulation. Both the CEL and AEL are set to 10 ~ 50 μm with a junction layer of 2.7 nm and two additional diffusion boundary layers of 20 μm. The operating mode was set in reverse bias.

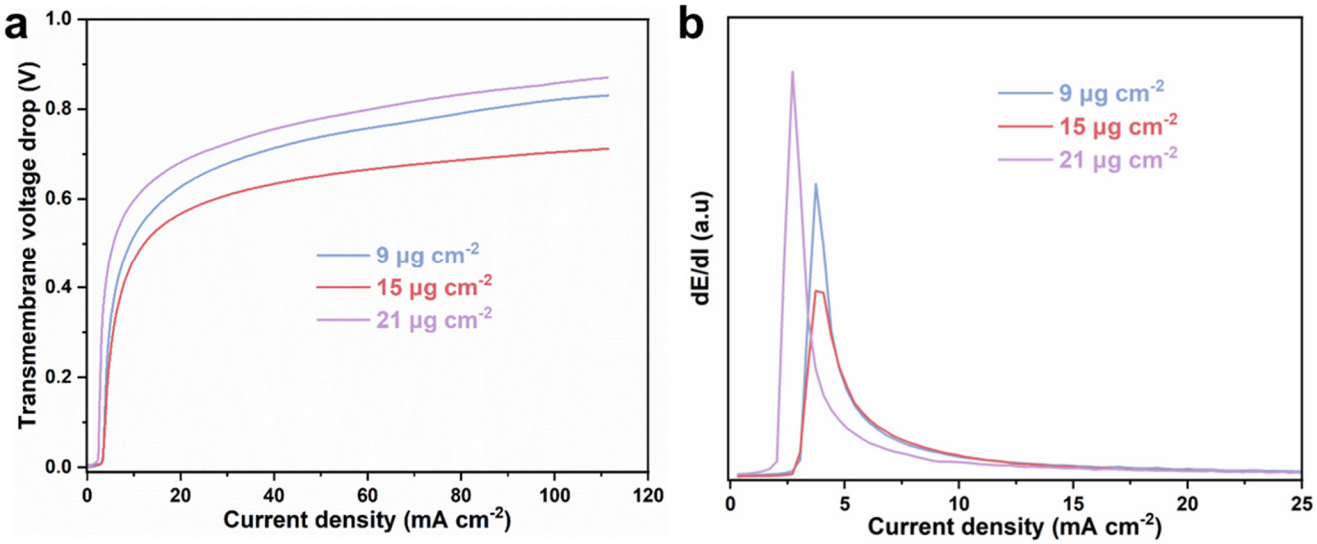

Fig. S13. (a) The I-V curves for BPMs with different loadings of GO-NCA junctional catalysts at low current density (0-100 mA cm^{-2}). (b) The derivative of dE/dI versus the current density for the BPMs corresponding to (a).

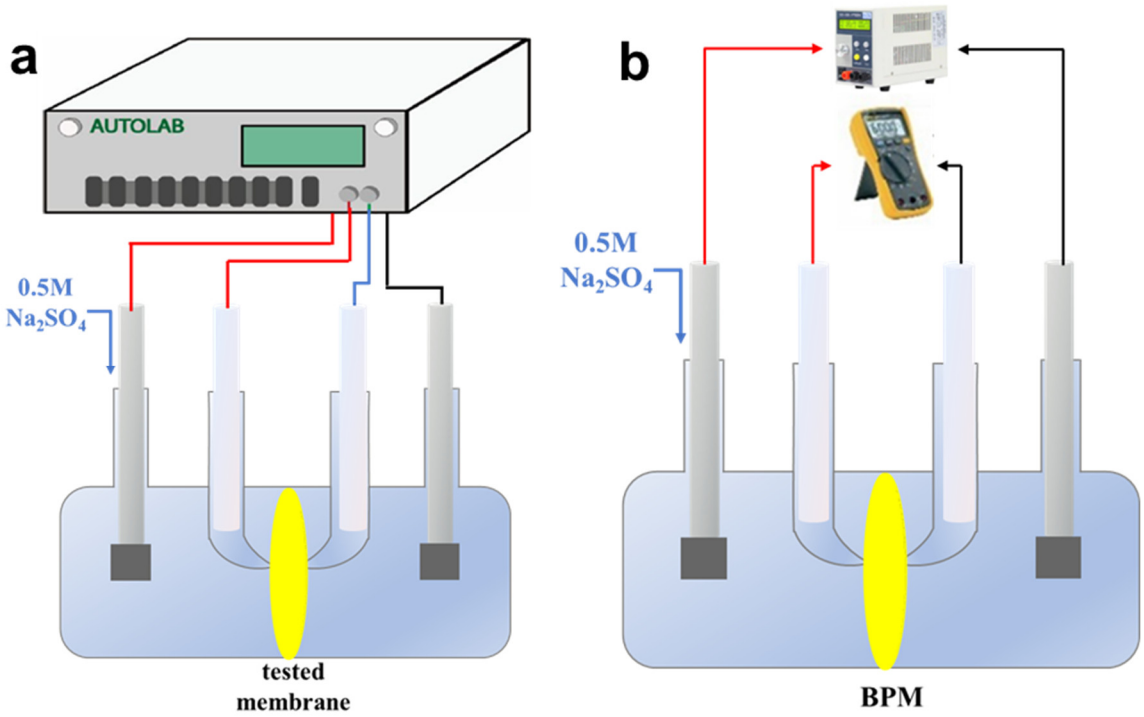

Fig. S14. (a) Configuration of four-electrode electrochemical cell for I-V relationship at low current density and EIS measurements. Herein, the electrochemical response of the surface and the junctions of BPMs stuck in the middle of two symmetrical compartments was assessed using a Kelvin four-point sensing electrochemical cell connected with an AUTOLAB workstation. Two platinum sheet electrodes placed outboard work as working (W) and counter (C) electrodes, whereas a pair of Ag/AgCl electrodes located approximately 1 mm on both sides of the BPM through Haber-Luggin capillaries act as the reference (R) and sense (S) electrodes. (b) Configuration of four-electrode electrochemical cell for I-V relationship and long-term WD stability at high current density. The testing methods and setup are similar to (a). Due to working at high current densities beyond the voltage limitations of the AUTOLAB workstation, the W and C electrodes connect with DC power supply, and the R and S electrodes link with a multimeter to record the transmembrane voltage. During long-term operation, electrolytes on both sides are continuously circulated and refreshed to mitigate the effects of polarization.

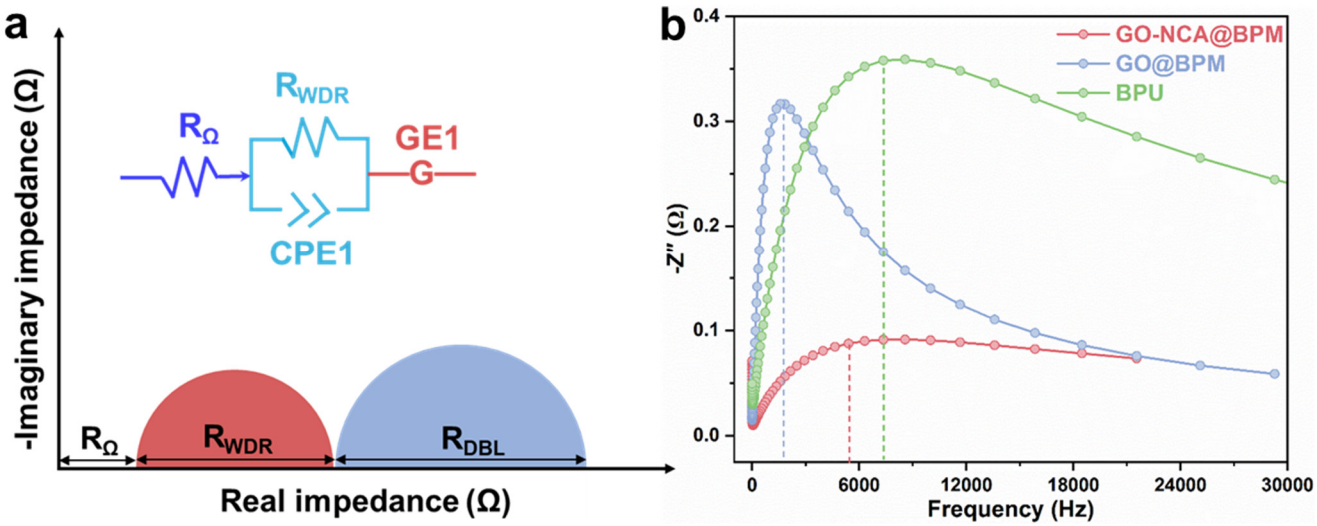

Fig. S15. (a) Schematic diagram of the equivalent circuit of BPM water dissociation, where R_{Ω}, R_{WDR}, CPE1 and GE1 represent the total Ohmic resistance of membrane layers, WD resistance, constant phase element, and Gerischer element, respectively. (b) Bode plots of BPMs at 20 mA cm^{-2}.

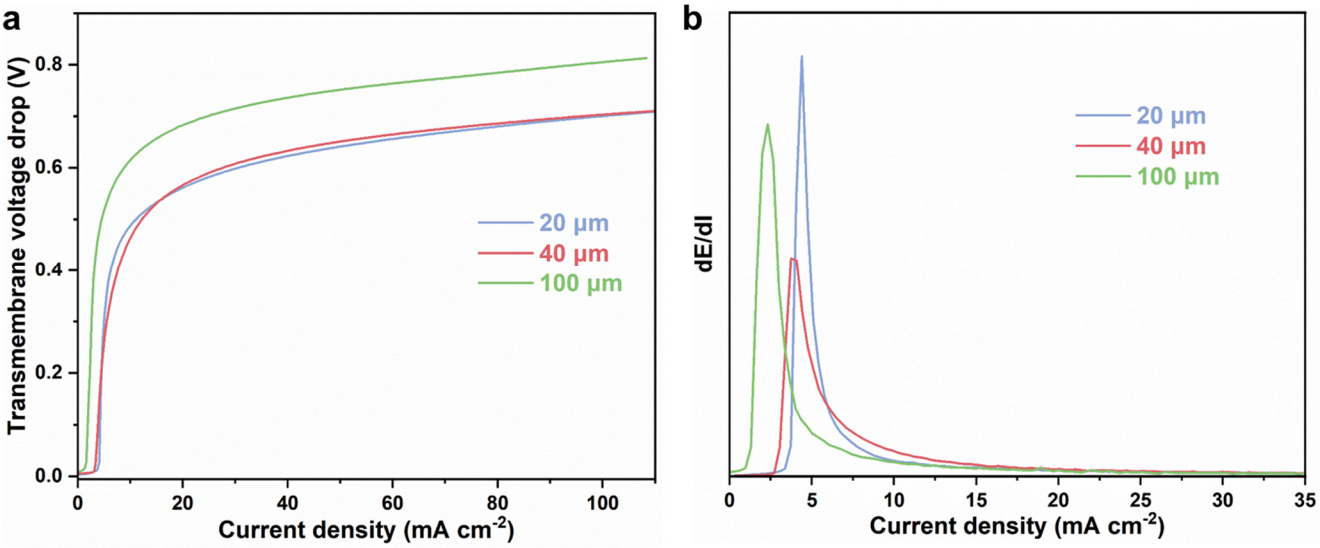

Fig. S16. (a) I-V curves for BPMs containing GO-NCA catalysts with different thickness at current density of 0-100 mA cm^{-2}. (b) The derivative of dE/dI versus the current density for three BPMs containing GO-NCA catalysts with different thickness.

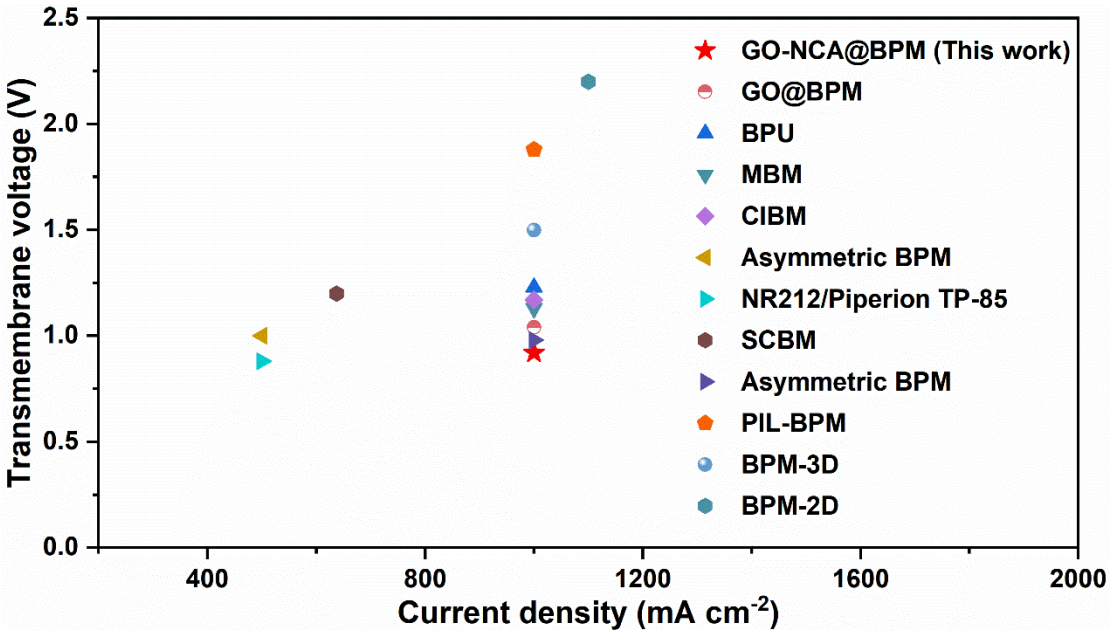

Fig. S17. Comparison of transmembrane voltage between previously reported BPMs and GO-NCA@BPM at high current densities.

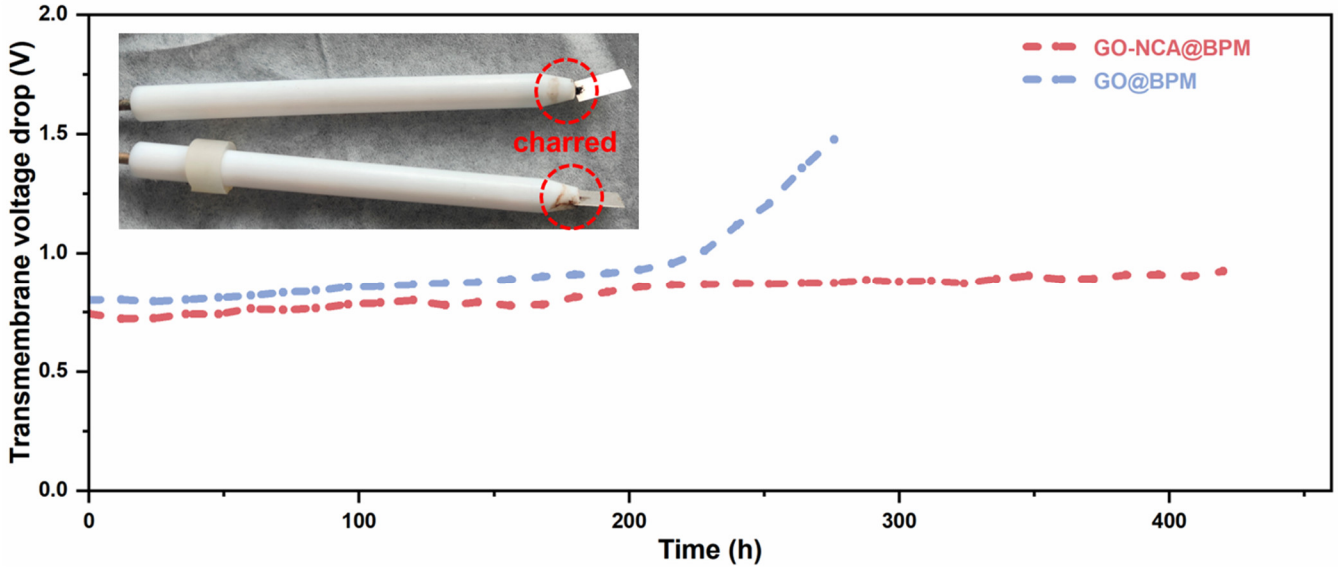

Fig. S18. The long-term WD stability of BPMs in the H-cell at 200 mA cm^{-2}. The inset shows the charred Pt electrodes at current densities exceeding 200 mA cm^{-2}. The GO-NCA@BPM operates steadily for over 420 hours, exhibiting only a voltage increment of 0.45 mV h^{-1}, which is approximately 5.6 times superior to GO@BPM (2.52 mV h^{-1}).

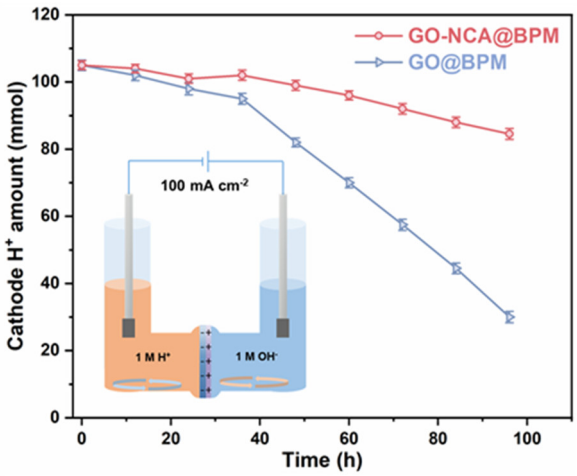

Fig. S19. Acid-base diffusion experiment for GO-NCA@BPM and GO@BPM in asymmetric electrolytes ((–) cathode|1 M H^+|BPM|1 M OH^-|anode (+)). A constant current density of 100 mA cm^{-2} was applied in reverse across the BPMs positioned between the compartments of an H-Cell, with 0.5 M H_2SO_4 on one side and 1 M KOH on the other. The H^+ amounts in the cathode compartment was monitored over time and quantified by titration.

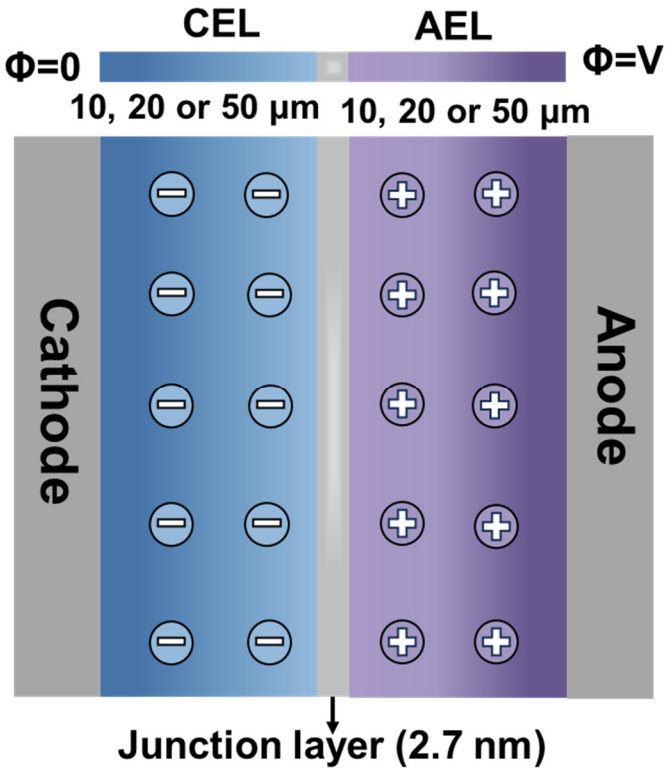

Fig. S20. Schematic illustration of 1-D BPM model in membrane electrode assembly (MEA) system for numerical simulation. Both the CEL and AEL are set to 10 ~ 50 μm with a junction layer of 2.7 nm. Due to the zero-gap configuration of MEA, there is no diffusion layer.

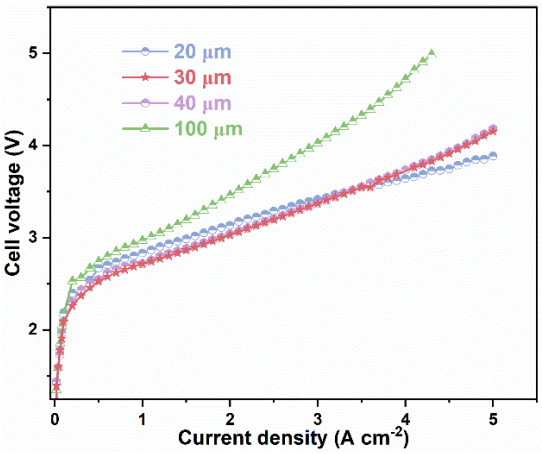

Fig. S21. Polarization curves of water electrolyzers assembled with GO-NCA@BPMs of different thickness (20~100 μm).

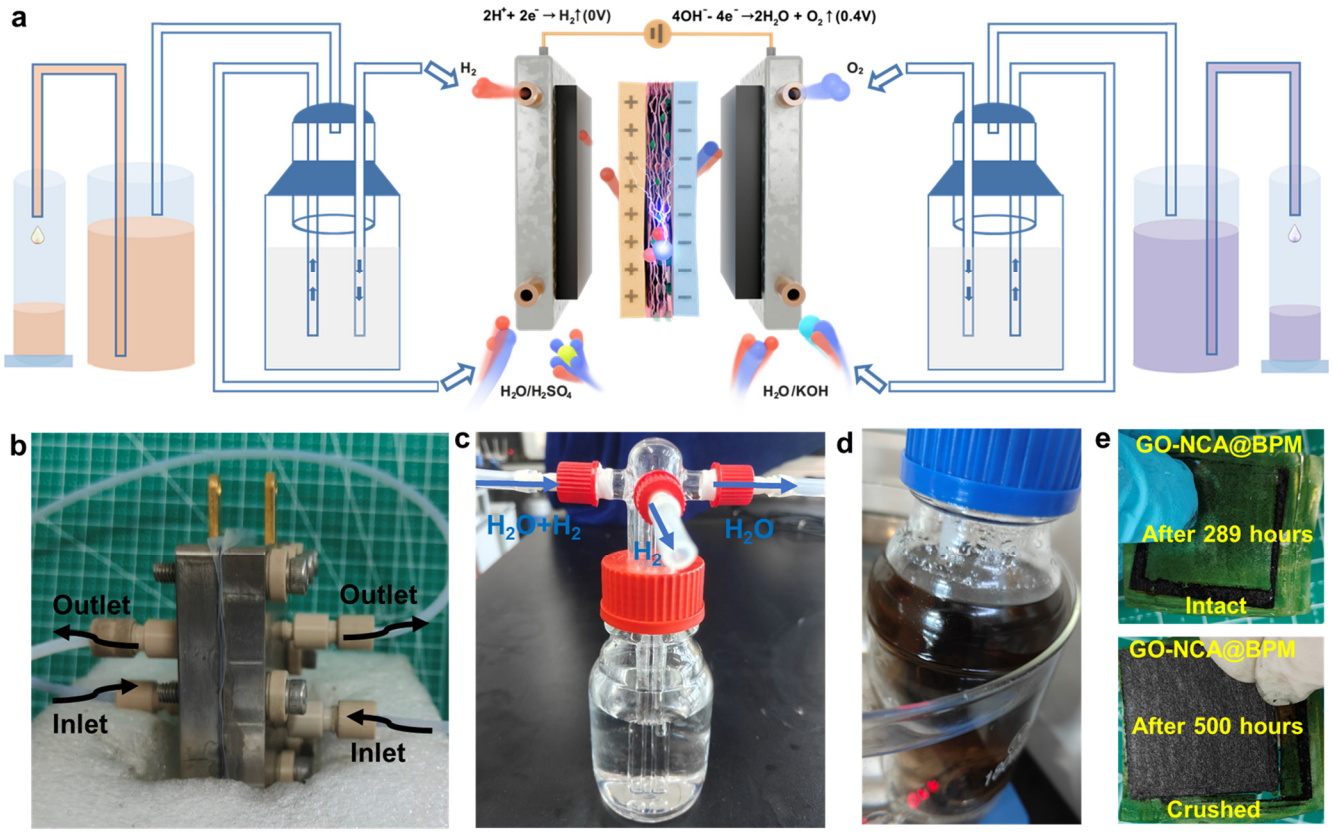

Fig. S22. Photography description of the BPM flow-cell water electrolyzer device. (a) Schematic of MEA and electrolyzer for collecting H_2 and O_2. The electrolyzer is made up of two Ti serpentine flow fields as the endplates, two PTFE gaskets and two gas diffusion layers, where BPM is stuck between anode and cathode GDLs (AEL toward the anode and CEL faces the cathode). Pure water is circulated to both the anode and cathode side through a double-channel peristaltic pump to feed the BPM via the GDLs. (b) Photograph of the flow-cell water electrolyzer setup. In this configuration, water is circulated through the system with distinct flow directions: the water flows downward on one side and upward on the other. (c) Photograph of the double inlet buffer bottle for gas collection. (d) Photograph of the feed solution in the anode after the 500-hour electrolytic water stability test. Notably, a severe detachment of IrO_2 catalysts from anode GDL can be observed in the bottle containing the anode feed solution. (e) Photographs of GO-NCA@BPM after the 289-hour test (above) and the 500-hour test (below) for electrolytic water stability. The GO-NCA@BPM remained intact after the 289-hour electrolytic water stability test. Unfortunately, after repeated disassembly and assembly of the membrane electrode assembly, the GO-NCA@BPM was ultimately crushed by the fixture after 500 hours.

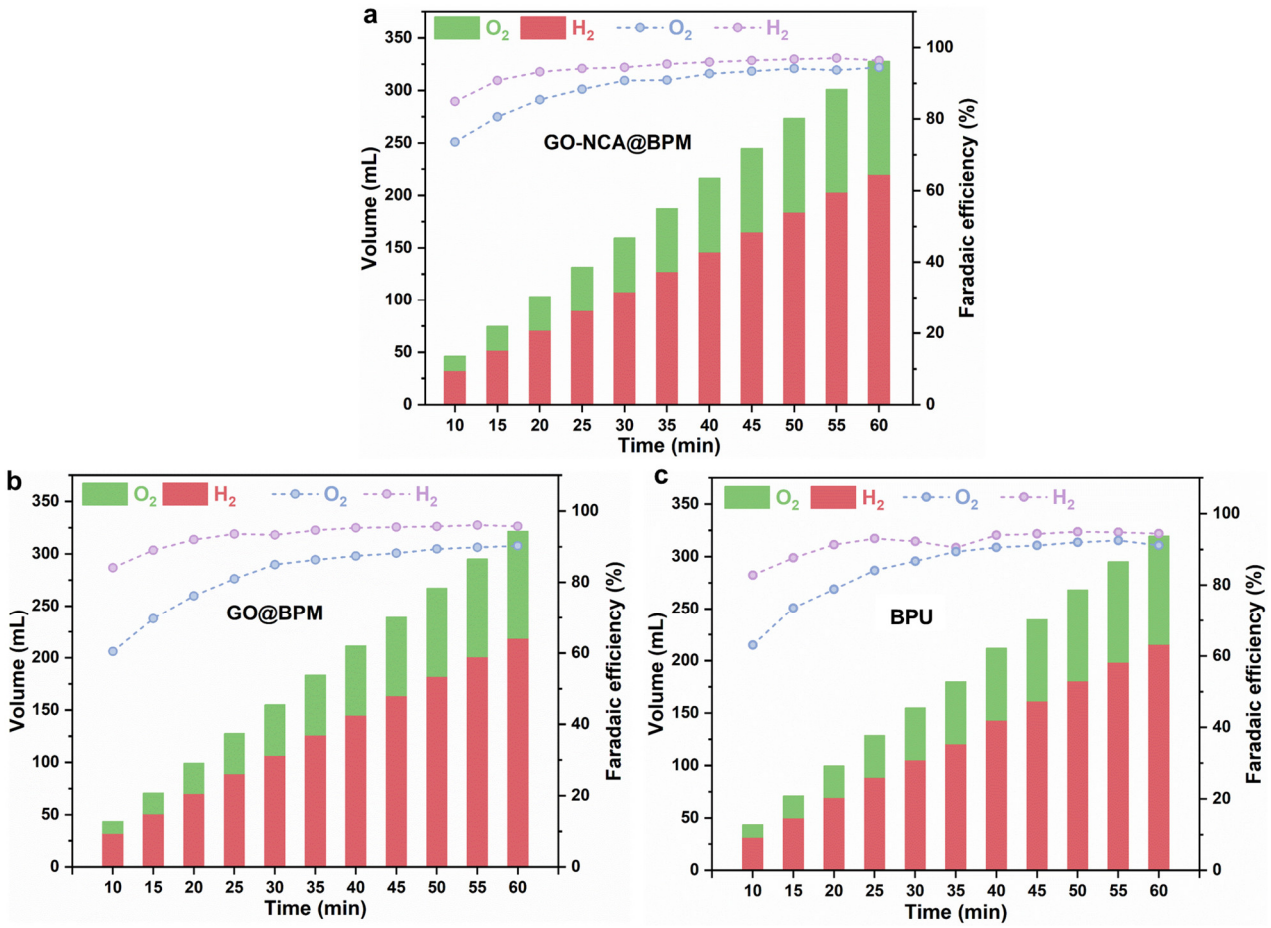

Fig. S23. Faradaic efficiency and the volume of actual gas. (a-c) The volume (left Y axis) and Faradaic efficiency (right Y axis) of H_2 and O_2 generated by the electrolyzer equipped with GO-NCA@BPM, GO@BPM and BP-1 at 500 mA cm^{-2} for an hour, respectively. The Faradaic efficiency is calculated via the equations S13-S16.

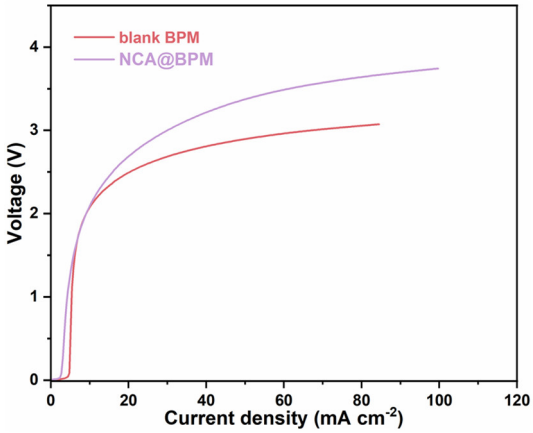

Fig. S24. I-V curves for BPMs before and after the incorporation of NCA molecules. NCA@BPM refers to the BPM containing 0.18 mg cm^{-2} of NCA molecules, while the blank BPM does not contain any NCA molecules. Notably, the WD voltage significantly increased after incorporating the NCA molecules into the BPM interlayer, indicating that the individual NCA molecules exhibit poor catalytic activity.

Table S1. The atomic ratio of GO and GO-NCA in XPS spectra.

Sample	C/%	O/%	N/%
GO	71	27.3	1.7
GO-NCA	52.8	39.2	8

Table S2. Modeling parameters.

Parameter	Description	Value
$L_{AEL/CEL}$	Membrane thickness	10, 20, 50 (µm)
IEC	ion exchange capacity	1.85 for CEL, 2.12 for AEL (mmol g^{-1})
$\rho_{M.\ wet}$	Density of the hydrated membrane	1.0 (g mL^{-1})
L_{char}	Characteristic bond length for WD	0.58 (nm)
L_{sdl}	Diffusion boundary	20 (µm)
c_0	Initial electrolytes concentration (Na_2SO_4)	0.5 (mol L^{-1})
Φ_0	Initial cell voltage	0 (V)
Kw_0	Water dissociation constant at zero field	10.64×10^{-14} ($m^3\ s^{-1}\ mol^{-1}$)
Kw_r	Backward rate constant water dissociation	5.20×10^{11} ($m^3\ s^{-1}\ mol^{-1}$)
T	Temperature	298.15 K
A	Wien effect coefficient	0.5 ($K^2\ m\ V^{-1}$)
D_{H^+}	Diffusivity	6.96×10^{-9} ($m^2\ s^{-1}$)
D_{OH^+}	Diffusivity	4.96×10^{-9} ($m^2\ s^{-1}$)
D_{Na^+}	Diffusivity	1.33×10^{-9} ($m^2\ s^{-1}$)
$D_{SO4^{2-}}$	Diffusivity	1.07×10^{-9} ($m^2\ s^{-1}$)
ε_0	Vacuum permittivity	$8.85\times10^{-14}\frac{As}{Vm}$
ε_r	Relative permittivity	35
q	Elementary charge	1.6×10^{-19} C

Table S3. Comparison of this work, recently reported and commercial BPMs based on energy efficiency (indicated by the transmembrane voltage drop at 100 mA cm^{-2}, U100) and selectivity (indicated by the 1st limiting current density).

BPM	1st limiting current density (mA cm^{-2})	U100 (V)	Electrolytes	Ref
BP-1	3.42	0.84	0.5 M Na_2SO_4	Commercial
GO-NCA@BPM	3.64	0.7	0.5 M Na_2SO_4	This work
GO@BPM	4.11	0.85	0.5 M Na_2SO_4	This work
GO-NCA@BPM (21 μg cm^{-2})	2.69	0.86	0.5 M Na_2SO_4	This work
GO-NCA@BPM (9 μg cm^{-2})	3.69	0.82	0.5 M Na_2SO_4	This work
SBM-NC2.0	5	1.4	0.5 M Na_2SO_4	13
SBM-D1.0	1.22	2.4	0.5 M Na_2SO_4	13
HBM-SG10	2.4	4.3	0.5 M NaCl	14
SCBM	6	1.1	0.5 M NaCl	15
CIBM	3.43	1.1	0.5 M Na_2SO_4	16
PIL-BPM-6h	10	1.87	1 M Na_2SO_4	17
Co-electrospun 3D BPM	5	1	0.5 M Na_2SO_4	18
Fe(III)@PEI-BPM	25	1.8	0.5 M Na_2SO_4	19
BPM-E3	9	4	0.5 M NaCl	20
MBM	4	0.76	0.5 M Na_2SO_4	21
0.5hFCBM	5.4	0.77	0.5 M Na_2SO_4	6
LBL Interface BPM	8	3.3	0.5 M NaCl	22
Intermediate BPM	7	3.9	0.5 M NaCl	22
PVA-CMC BPM	10	5.6	0.5 M NaCl	23

Table S4. The results of EIS simulation.

Name	GO-NCA@BPM	GO@BPM	BP-1
R_Ω (Ω)	0.057	0.057	0.406
R_{WDR} (Ω)	0.25	0.76	0.36
k_d (s^{-1})	0.57	0.16	0.35
τ_{tr} (μs)	19.23	93.46	14.67
E^*10^8 (V m^{-1})	9.66	8.46	9.19
χ^2	0.0026	0.0265	0.0053

Table S5. Comparation of BPM water electrolyzer performance.

System	Temperature (°C)	Current density (mA cm^{-2})	Cell voltage (V)	Ref.
Pure water	80	5000	4.1	This work
	80	1000	2.7	
0.5 M H_2SO_4 (for cathode),	80	6500	3.9	This work
1 M KOH (for anode)	80	1000	1.9	
1 M H_2SO_4 (for cathode), 2 M NaOH (for anode)	25	160	2.31	24
Pure water	50	500	2.2	8
Pure water	55	1000	2.1	25
Pure water	50	3400	4	26
Pure water	55	500	2	27
Pure water	55	500	2.5	28
Pure water	80	450	2.2	29
Pure water	50	500	4.6	30
Pure water	50	500	2.6	31
Pure water (for anode), 0.5 M NaCl (for cathode)	50	500	3.5	31

Table S6. Comparation of BPM electrolyzer stability.

System	Temperature (°C)	Current density (mA cm^{-2})	Operating time (h)	Ref
Pure water	60	500	500	This work
1 M H_2SO_4 (for cathode), 2 M NaOH (for anode)	25	20	12	24
Pure water	55	1000	100	25
Pure water	50	1000	4	26
Pure water	55	500	60	28
Pure water	50	500	5	30
1 M KOH, 2000 ppm KNO_3 (NH_3 electrosynthesis)	–	1000	110	21
1 M KOH, 2000 ppm KNO_3 (NH_3 electrosynthesis)	–	1000	210	16
1 M KOH, 3 M $KHCO_3$ (CO_2 reduction)	–	100	2.5	32
3 M KOH, 1.5 M K_2CO_3 (CO_2 reduction)	–	300	25	33

Table S7. Comparison of the water dissociation performance of BPMs at high current densities.

BPM	Electrolytes	Current density (mA cm^{-2})	Voltage (V)	Ref
GO-NCA@BPM	0.5 M Na_2SO_4	1,000	0.92	This work
GO@BPM	0.5 M Na_2SO_4	1,000	1.04	This work
BPU	0.5 M Na_2SO_4	1,000	1.23	Commercial
MBM	0.5 M Na_2SO_4	1,000	1.13	21
CIBM	0.5 M Na_2SO_4	1,000	1.17	16
Asymmetric BPM	0.5 M NaCl	500	1	26
NR212/Piperion TP-85	0.5 M NaCl	500	0.88	34
SCBM	0.5 M NaCl	637	1.2	15
Asymmetric BPM	0.5 M NaCl	1,000	0.98	26
PIL-BPM	1 M Na_2SO_4	1,000	1.88	17
BPM-3D	0.5 M Na_2SO_4	1,000	1.5	35
BPM-2D	0.5 M Na_2SO_4	1100	2.2	35

References

1. W. Yu, Z. Ge, K. Zhang, X. Liang, X. Ge, H. Wang, M. Li, X. Shen, Y. Xu, L. Wu, T. Xu, *Ind. Eng. Chem. Res*. 2022, **61**, 4329-4338.
2. W. Song, K. Peng, W. Xu, X. Liu, H. Zhang, X. Liang, B. Ye, H. Zhang, Z. Yang, L. Wu, X. Ge, T. Xu, *Nat. Commun*. 2023, **14**, 2732.
3. Z. Wang, L. Huang, X. Dong, T. Wu, Q. Qing, J. Chen, Y. Lu, C. Xu, *Nat. Commun*. 2023, **14**, 261.
4. C. D. Gutsche, K. C. Nam, *J. Am. Chem. Soc.* 1988, **110**, 6153-6162.
5. W. Yu, C. Wei, K. Zhang, Z. Ge, X. Liang, M. D. Guiver, X. Ge, L. Wu, T. Xu, *Environ. Sci. Technol*. 2023, **14**, 5861-5871.
6. Z. Ge, M. A. Shehzad, X. Yang, G. Li, H. Wang, W. Yu, X. Liang, X. Ge, L. Wu, T. Xu, J. *Membr. Sci.* 2022, **656**, 120660.
7. B. S. Kim, S. C. Park, D. H. Kim, G. H. Moon, J. G. Oh, J. Jang, M-S. Kang, K. B. Yoon, Y. S. Kang, *Small* 2020, **16**, 2002641.
8. S. Z. Oener, M. J. Foster, S. W. Boettcher, *Science* 2020, **369**, 1099–1103.
9. Z. Yan, L. Zhu, Y. C. Li, R. J. Wycisk, P. N. Pintauro, M. A. Hickner, T. E. Mallouk, *Energy Environ. Sci*. 2018, **11**, 2235-2245.
10. O. Weiland, P. Trinke, B. Bensmann, R. Hanke-rauschenbach, *J. Electrochem. Soc.* 2023, **170**, 054505.
11. J. C. Bui, E. W. Lees, D. H. Marin, T. N. Stovall, L. Chen, A. Kusoglu, A. C. Nielander, T. F. Jaramillo, S. W. Boettcher, A. T. Bell, A. Z. Weber, *Nat. Chem. Eng*. 2024, **1**, 45-60.
12. Y. Zheng, W. Ma, A. Serban, A. Allushi, X. Hu, *Angew. Chem. Int. Ed.* 2024, DOI: 10.1002/anie.202413698.
13. B. Eswaraswamy, A. Suhag, P. Goel, P. Mandal, S. Chattopadhyay, *Sep. Purif. Technol*. 2022, **295**, 121257.
14. B. Eswaraswamy, P. Goel, P. Mandal, A. Chandra, S. Chattopadhyay, *Polym. Adv. Technol.* 2022, **33**, 353-367.
15. M. A. Shehzad, A. Yasmin, X. Ge, Z. Ge, K. Zhang, X. Liang, J. Zhang, G. Li, X. Xiao, B. Jiang, L. Wu, T. Xu, *Nat. Commun*. 2021, **12**, 9.
16. Z. Xu, Y. Liao, M. Pang, L. Wan, Q. Xu, Y. Zhen, B. Wang, *Energy Environ. Sci*. 2023, **16**, 3815–3824.
17. G. Li, M. A. Shehzad, Z. Ge, H. Wang, A. Yasmin, X. Yang, X. Ge, L. Wu, T. Xu, *Sep. Purif. Technol*. 2021, **275**, 119167.
18. Y. Chen, J. A. Wrubel, W. E. Klein, S. Kabir, W. A. Smith, K. C. Neyerlin, T. G. Deutsch, *ACS Appl. Polym. Mater*. 2020, **2**, 4559-4569.
19. Z. Ge, M. A. Shehzad, L. Ge, Y. Zhu, H. Wang, G. Li, J. Zhang, X. Ge, L. Wu, T. Xu, *ACS Appl. Energy Mater.* 2020, **3**, 5765-5773.
20. E. Al-Dhubhani, H. Swart, Z. Borneman, K. Nijmeijer, M. Tedesco, J. W. Post, M. Saakes, *ACS Appl. Energy Mater*. 2021, **4**, 3724-3736.
21. Z. Xu, L. Wan, Y. Liao, M. Pang, Q. Xu, P. Wang, B. Wang, *Nat. Commun.* 2023, **14**, 1619.
22. S. Abdu, K. Sricharoen, J. E. Wong, E. S. Muljadi, T. Melin, M. Wessling, *ACS Appl. Mater. Interfaces* 2013, **5**, 10445-10455.
23. T. Zhou, Y. Hu, R. Chen, X. Zheng, X. Chen, Z. Chen, J. Zhong, *Appl. Surf. Sci.* 2012, **258**, 4023-4027.
24. L. Lee, D. Kim, *J. Mater. Chem. A* 2021, **9**, 5485-5496.
25. S. Sasmal, L. Chen, P. V. Sarma, O. T. Vulpin, C. R. Simons, K. M. Wells, R. J. Spontak, S. W. Boettcher, *Nat. Mater*. 2024, DOI: 10.1038/s41563-024-01943-8.
26. S. Z. Oener, L. P. Twight, G. A. Lindquist, S. W. Boettcher, *ACS Energy Lett*. 2020, **6**, 1-8.
27. L. Chen, Q. Xu, S. Z. Oener, K. Fabrizio, S. W. Boettcher, *Nat. Commun*. 2022, **13**, 3846.
28. Y-L. Kao, L. Chen, S. W. Boettcher, D. Aili, *ACS Energy Lett*. 2024, **9**, 2953-2959.
29. B. Mayerhöfer, D. Mclaughlin, T. Böhm, M. Hegelheimer, D. Seeberger, S. Thiele, *ACS Appl. Energy Mater*. 2020, **3**, 9635-9644.
30. S. K. Maiti, N. Ali, T. K. Maiti, A. Suhag, M. Ray, S. Chattopadhyay, *Int. J. Hydrogen Energy* 2024, **80**, 1062-1074.
31. D. H. Marin, J. T. Perryman, M. A. Hubert, G. A. Lindquist, L. Chen, A. M. Aleman, G. A. Kamat, V. A. Niemann, M. B. Stevens, Y. N. Regmi, S. W. Boettcher, A. C. Nielander, T. F. Jaramillo, *Joule* 2023, **7**, 765-781.
32. T. Li, E. W. Lees, M. Goldman, D. A. Salvatore, D. M. Weekes, C. P. Berlinguette, *Joule* 2019, **3**, 1487-1497.
33. G. Lee, A. S. Rasouli, B-H. Lee, J. Zhang, D. H. Won, Y. C. Xiao, J. P. Edwards, M. G. Lee, E. D. Jung, F. Arabyarmohammadi, H. Liu, I. Grigioni, J. Abed, T. Alkayyali, S. Liu, K. Xie, R. K. Miao, S. Park, R. Dorakhan, Y. Zhao, E. *Joule* 2023, **7**, 1277-1288.
34. É. Lucas, J. Bui, M. Hwang, K. Wang, A. Bell, A. Weber, S. Ardo, H. Atwater, C. Xiang, *ChemRxiv* 2023, DOI: 10.26434/chemrxiv-2023-n4c6x.
35. C. Shen, R. Wycisk, P. N. Pintauro, *Energy Environ. Sci.* 2017, 10, 1435–1442.